HEALTH AND MEDICINE

Particle-based artificial three-dimensional stem cell spheroids for revascularization of ischemic diseases

Ran Zhang[1], Wenya Luo[1], Yue Zhang[2], Dashuai Zhu[3], Adam C. Midgley[1], Hao Song[2], Anila Khalique[1], Haoqi Zhang[1,4], Jie Zhuang[1,3,4], Deling Kong[1]*, Xinglu Huang[1,4]*

Development of new approaches to biomimetically reconstruct vasculature networks remains challenging in regenerative medicine. We introduce a particle-based artificial stem cell spheroid (ASSP) technology that recapitulates paracrine functions of three-dimensional (3D) SSPs for vasculature regeneration. Specifically, we used a facile method to induce the aggregation of stem cells into 3D spheroids, which benefited from hypoxia microenvironment–driven and enhanced secretion of proangiogenic bioactive factors. Furthermore, we artificially reconstructed 3D spheroids (i.e., ASSP) by integration of SSP-secreted factors into micro-/nanoparticles with cell membrane–derived surface coatings. The easily controllable sizes of the ASSP particles provided superior revascularization effects on the ischemic tissues in hindlimb ischemia models through local administration of ASSP microparticles and in myocardial infarction models via the systemic delivery of ASSP nanoparticles. The strategy offers a promising therapeutic option for ischemic tissue regeneration and addresses issues faced by the bottlenecked development in the delivery of stem cell therapies.

INTRODUCTION

Ischemic diseases are a leading cause of global morbidity and mortality. Therapeutic strategies for ischemic diseases aim to reperfuse ischemic tissues through the regeneration of functional vasculature networks (*1*, *2*). In recent years, the use of stem cell–based therapeutics have gained substantial attention in the development of treatments for ischemic diseases (*3*–*5*), primarily by taking advantage of the paracrine mechanisms of stem cells (*6*, *7*). The multitude of proangiogenic bioactive factors secreted from stem cells [collectively known as "cocktail" factors (CFs)] can promote the endogenous repair of tissues afflicted with ischemia. However, several critical issues restrict the utilization of cellular approaches for ischemia therapy (*8*–*12*), such as extremely low cell retention and integration of engrafted cells, fairly limited delivery efficacy due to the entrapment of most of systemically administered cells within the lungs, the mechanical damage caused by the invasive injection process, and the low storage/shipping stability of live cells.

Recently, biomaterial-based cell delivery has shown promising directions to overcome the above barriers of cell-based therapy (*13*–*15*). For example, a smart strategy for preparation of materials mimicking some stem cell functions was developed by packaging secreted factors from in vitro culture of bone marrow–derived mesenchymal stem cells (MSCs) into poly(lactic-*co*-glycolic acid) (PLGA) particles (*16*). These synthetic MSC-like particles were shown to have similar therapeutic benefits to natural MSC therapy in various diseases (*17*–*19*). However, the paracrine release of factors from commonly used in vitro culture conditions does not adequately represent the paracrine components released from engrafted stem cells due to the three-dimensional (3D) physiological environment experienced by stem cells in the body (*20*), including but not limited to the intercellular interactions of engrafted stem cells. Until now, there are no reports that have attempted artificial reconstruction of particles with the biomimetic functionality of advantageous 3D MSC spheroid paracrine secretome.

Inspired by evidence of feasibility, we hypothesized that generation of artificial 3D MSCs could offer improved implantation survivability and therapeutic efficacy for ischemic diseases. Hence, we constructed 3D stem cell spheroids (SSPs) by inducing cell-cell aggregation through addition of a cell adhesion–modifying chemical. We then further evaluated the proangiogenesis capacity of SSPs based on hypoxia-mastering regulation of CF production. On the basis of the benefits of SSP in revascularization, we then proposed a conceptual design of artificial SSP (ASSP) analogs. In this system, the biomimetic ASSPs were prepared by integration of secreted CF from SSPs into micro-/nanoparticles, followed by coating the surface of the particles with cell membranes from different cell types, catered to disease treatment. The synthetic ASSPs showed various advantages over SSPs, especially in enabling access to different administration methods due to the freely controlled particle size. Here, we used mouse models of critical hindlimb ischemia (HI) and myocardial infarction (MI) to assess the therapeutic potential of ASSPs by local transplantation of ASSP microparticles (ASSP-MPs) and intravenous delivery of targeted ASSP nanoparticles (ASSP-NPs), respectively.

RESULTS

Construction of 3D SSPs

Before preparation of SSPs, adipose tissue–derived MSCs (aMSCs) were isolated and cultured using our previously described methods (*21*, *22*). Identification of aMSCs was performed by flow cytometry analysis of typical surface markers and evaluation of the ability to successfully differentiate into osteocytes and adipocytes (fig. S1). The scheme of SSP preparation is outlined in Fig. 1A. Following optimization (fig. S2), the surface of aMSCs was modified by Arg-Gly-Asp (RGD)–conjugated eight-armed polyethylene glycol (8-PEG-RGD) before

[1]Key Laboratory of Bioactive Materials, Ministry of Education, College of Life Sciences, and State Key Laboratory of Medicinal Chemical Biology, Nankai University, Tianjin 300071, China. [2]Department of Physiology and Pathophysiology, Tianjin Medical University, Tianjin 300070, China. [3]College of Medicine, Nankai University, Tianjin 300071, China. [4]Joint Laboratory of Nanozymes, College of Life Sciences, Nankai University, Tianjin 300071, China.
*Corresponding author. Email: huangxinglu@nankai.edu.cn (X.H.); kongdeling@nankai.edu.cn (D.K.)

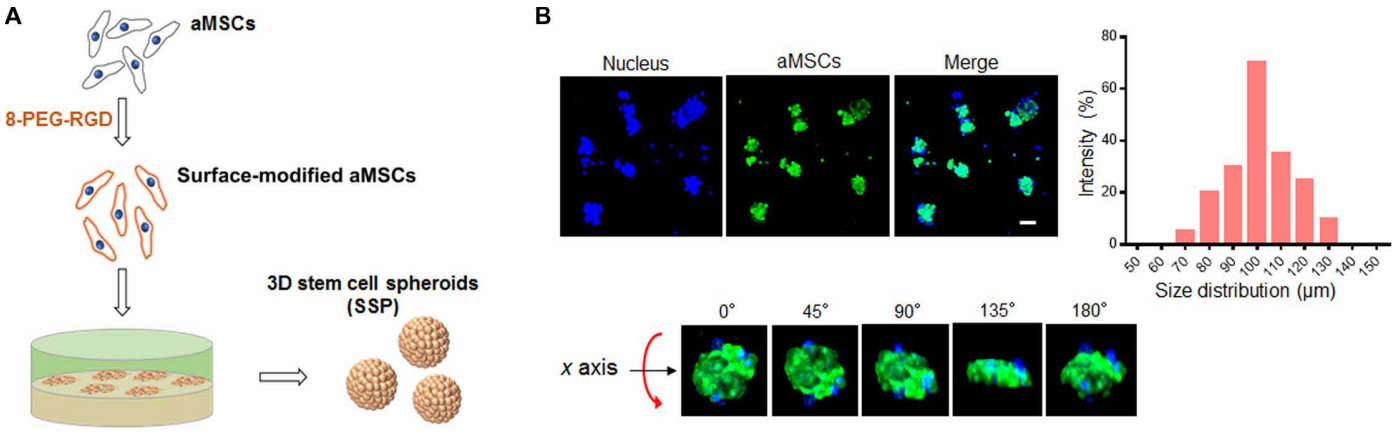

Fig. 1. Construction of 3D SSPs. (**A**) Scheme of preparation of 3D SSPs via use of 8-PEG chemical modification strategy. (**B**) Representative images of 3D SSPs (left image) and size distribution of 3D SSPs (right-hand graph). Z-stack reconstructed confocal images of 3D SSPs at different angles along *x*-axis rotation (bottom). Scale bar, 100 μm.

cell culture on agarose gel, to induce 3D aggregation growth. In this process, 8-PEG-RGD provided cell-cell junction due to highly expression of integrin on aMSC surface (*23*), an RGD-specific binding ligand (*24*). Surface modification with RGD was able to inhibit cell adhesion to matrix/culture substrate by blocking integrin interactions (*25*). Furthermore, the agarose gel also guaranteed free migration of the cells by destroying cell attachment to substrate. Confocal microscopy was used to assess preferential cell growth toward aggregation, and 3D structure was further confirmed by analyzing the Z-stack reconstructed images along *x*-axis rotation (Fig. 1B). Quantification analysis revealed that the size distribution of the resulting SSPs was mainly in the range of 70 to 130 μm.

Hypoxic microenvironment of 3D SSPs promoted CF secretion for improved revascularization

We next sought to explore the advantages of CF secreted from 3D SSPs. The schematics for culture design for preparation of CF-containing medium secreted from 2D cultured aMSCs (2D-CF) and 3D-CF is summarized in Fig. 2A. Briefly, plating cells for 2D or 3D culture were performed in serum-free medium. After 5 days of culture, the medium was collected for further analysis. SDS–polyacrylamide gel electrophoresis (PAGE) of conditioned medium taken from each culture model revealed enriched protein abundance in 3D-CF compared to 2D-CF, and the stem cell culture medium used did not affect this result. Given that there was no observed significant difference in cell number between 2D and 3D cultures (fig. S3), the results demonstrated that stem cells in 3D structure promoted CF secretion. To further evaluate different cell structure–induced changes in protein composition of CF, we performed liquid chromatography–mass spectrometry (LC-MS) proteomic analysis and compared differences in protein content between 2D-CF and 3D-CF. Differentially expressed proteins were defined as those in which the average label-free quantification (LFQ) intensity for each group exceeded a twofold change, with a *P* value of less than 0.05. Furthermore, an unsupervised enrichment analysis between the two groups of differentially expressed proteins was examined using the Kyoto Encyclopedia of Genes and Genomes (KEGG) pathway database. The results showed a significant enrichment of 14 signaling pathways, and the hypoxia-inducible factor–1 signaling pathway (i.e., hypoxia related) was the third most significantly enriched signaling pathway (Fig. 2B and fig. S4). It has been reported that hypoxia is a key regulator for mastering the secretion of angiogenesis factors (*26*, *27*). Hypoxic conditions commonly afflict the inner cells of 3D cell spheroids, due to limited oxygen diffusion (*28*). Thus, we explored whether 3D SSPs generated by stem cell aggregation had hypoxic status, and subsequently, the slices from 3D SSPs were stained using a hypoxyprobe (pimonidazole), which is reductively and specifically activated in hypoxic cells, allowing for immunofluorescent visualization. Figure 2C confirms hypoxia occurrence according to the presence of green fluorescence (pimonidazole-stained hypoxia) within centralized cells of the spheroids. Following analysis of factors involved in several key stem cell–mediated functions (angiogenesis, inflammation, and apoptosis), vascular regeneration–associated proteins were the topmost elevated proteins identified in 3D-CF compositions, in comparison to 2D-CF (Fig. 2D). These proteins included vascular endothelial growth factor (VEGF), epidermal growth factor (EGF), hepatocyte growth factor, platelet-derived growth factor, angiopoietin-1, and erythropoietin. This was especially true for VEGF, as the secreted amount by 3D SSPs was 12.9-fold higher than that of 2D-cultured aMSC (2D-aMSC) cultures. Vessel formation is a sequential process that is highly controlled via numerous factors, and thus, we further confirmed the difference of the mRNA expression in 2D cells and 3D SSPs. The representative factors contained in 3D SSPs were higher than that of 2D cells, as shown by analysis of mRNA expression levels of factors involved in revascularization ($P < 0.01$) (Fig. 2E).

The above results provide a rationale for use of 3D-CF as an amalgamation of effector molecules for proangiogenesis therapy. Therefore, we next assessed and compared the capacity for 2D-CF and 3D-CF in stimulating human umbilical vein endothelial cell (HUVEC) migration. Transwell assays were set up, and CF secreted from equivalent numbers of stem cells was added to the bottom well (Fig. 2F). Compared to the cells with an absence of CF and cells presented with 2D-CF, there was a noticeable improvement in the migration ability of HUVECs from the top well to the bottom well observed when cells were presented with 3D-CF ($P < 0.01$). Furthermore, according to the tube formation assay, the vessel formation capacity of the HUVECs treated with 2D-CF and 3D-CF were significantly elevated in comparison to untreated cells ($P < 0.01$), and the HUVEC-lined vessels after treatment with 3D-CF were 11.5 ± 1.6– and 3.2 ± 0.7–fold longer than that of untreated and 2D-CF–treated cells, respectively (Fig. 2G).

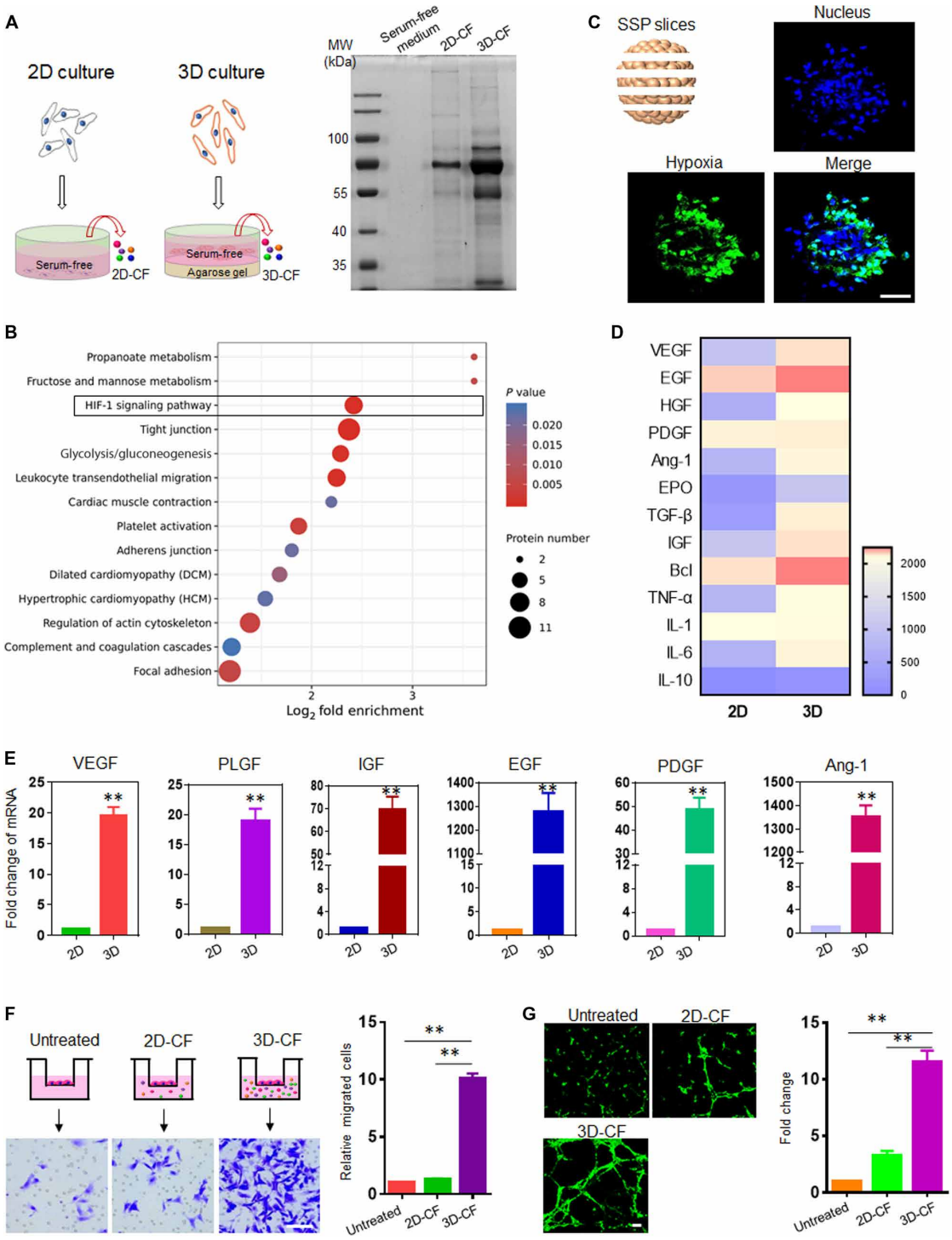

Fig. 2. Properties of 3D SSPs and its secretion factors. (**A**) SDS-PAGE analysis of secreted factors from aMSCs and 3D SSPs. The secreted factors from aMSCs (i.e., 2D-CF) and 3D SSPs (i.e., 3D-CF) cultured in serum-free medium were collected as described in the scheme (left). MW, molecular weight. (**B**) Increased fold change of 3D-CF in the related functions compared to that of 2D-CF by an unsupervised enrichment analysis of KEGG pathway based on LC-MS proteomic method. HIF-1, hypoxia-inducible factor–1; HGF, hepatocyte growth factor; PDGF, platelet-derived growth factor; Ang-1, angiopoietin-1; EPO, erythropoietin; TGF-β, transforming growth factor–β; TNF-α, tumor necrosis factor–α; IL-1, interleukin-1. (**C**) Representative images of hypoxic cells (green) in 3D SSPs by immunostaining of cryosections with hydroxyprobe (pimonidazole). Scale bar, 50 μm. (**D**) Heat map of proteins differentially expressed in 2D-CF and 3D-CF, based on LC-MS proteomic analysis. (**E**) Comparison of mRNA expression level of various proangiogenesis factors in 2D cells and 3D SSPs. $^{**}P < 0.01$. (**F**) Transwell assay analysis of migration capacity of human umbilical vein endothelial cells (HUVECs). HUVECs were plated onto upper wells, and the medium containing CF was added into bottom wells. Scale bar, 100 μm. $^{**}P < 0.01$. (**G**) Tube formation assay of HUVECs with or without 2D-CF and 3D-CF treatments. Scale bar, 100 μm. $^{**}P < 0.01$. All data are presented as means ± SEM. A two-tailed, unpaired Student's *t* test was used to compare between any two groups. One-way analysis of variance (ANOVA) was used to compare between three or more groups.

Reconstruction of artificial 3D SSP using PLGA microparticles

As illustrated in Fig. 3A, the conceptual design of ASSP preparation was the loading of 3D-CF into PLGA microparticles (ASSP-MPs), followed by coating with cell membrane extracted from 3D SSPs. Scanning electron microscopy and fluorescence imaging confirmed the successful coating of SSP cell membrane on the microparticle surface and that protein was loaded into the microparticles (Fig. 3, B and C). The size of ASSP-MPs was slightly increased compared to blank PLGA-MP alone and similar to the size of aMSCs (Fig. 3D). Flow cytometry analysis showed that the surface marker expression of ASSP-MPs was comparable to those of aMSCs, whereas the PLGA-MPs were negative for the markers (Fig. 3E and fig. S5, A and B). In addition, the CF loading efficiency into ASSP-MPs was approximately 49% of the total input CF. Sustained release kinetics of CF was observed by time-course analysis of ASSP-MPs incubated in phosphate-buffered saline (PBS) solution (Fig. 3F). To further understand the differential release dynamics of ASSP-MP–loaded components, three typical proangiogenesis factors [VEGF, EGF, and insulin-like growth factor (IGF)] were analyzed for their release into solution by enzyme-linked immunosorbent assay (ELISA). Figure 3G showed that the three factors are detectable, with slow release kinetics more than 6 days. Furthermore, it was apparent that a considerably higher concentration of IGF had been loaded into ASSP-MPs than both VEGF and EGF according to the release curves.

We next sought to explore the advantages of ASSP-MPs over living stem cells. The unresolved issue of manufacturability of living stem cell products is the low storage/shipping stability of the cells. We, thus, studied the stability of ASSP-MPs following freezing/thawing process. Cryopreservation did not significantly alter the size, the membrane coating, surface marker expression, or the dynamic release of CF (fig. S6, A to D). The survival/retention of aMSCs in

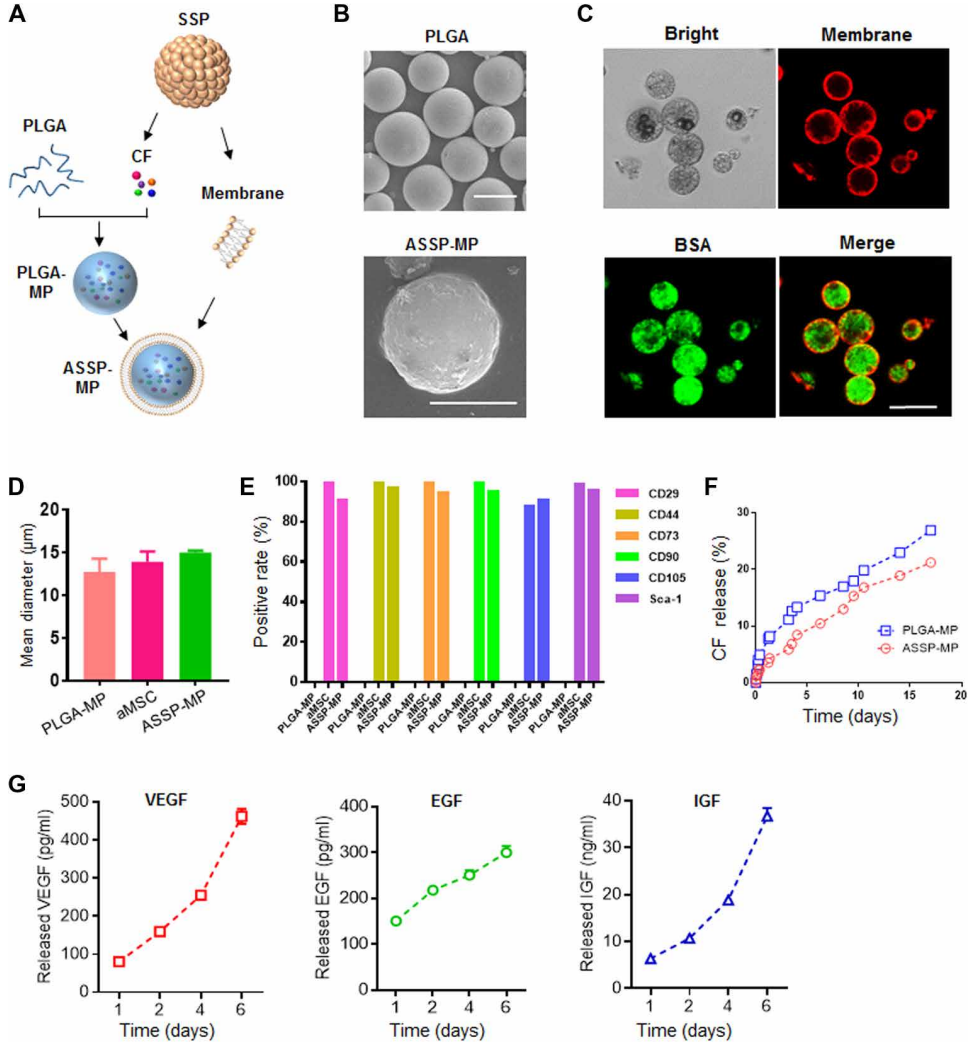

Fig. 3. Preparation and characterization of ASSP-MPs. (**A**) Schematic illustration of preparation of ASSP-MPs. ASSP-MPs were fabricated by loading CF secreted from SSPs into PLGA-MPs, and then PLGA-MPs were coated with cell membrane fragments of SSPs to form ASSP-MPs. (**B**) Scanning electron microscopy images of PLGA-MPs (top) and ASSP-MPs (bottom). Scale bars,10 μm. (**C**) Representative images of the structure of ASSP-MPs; bovine serum albumin (BSA)–fluorescein isothiocyanate (FITC) was loaded into PLGA-MPs (green), and cell membranes were labeled with DiD dyes (red). Scale bar, 20 μm. (**D**) Quantification analysis of mean diameter and (**E**) quantification analysis of expression of aMSC surface markers of PLGA-MPs (negative control), aMSCs, and ASSP-MPs. (**F**) CF release kinetics from PLGA-MPs and ASSP-MPs incubated in PBS solution. (**G**) Release kinetics of three typical proangiogenesis factors from ASSP-MPs over time based on ELISA analysis.

engraftment sites determines therapeutic index due to their paracrine mechanisms. Next, we compared the survival/retention of aMSCs and ASSP-MPs following local administration into ischemic tissue in a mouse acute HI model. This was determined by assessing signal decay of luciferase-expressing aMSCs and Cy5-labeled bovine serum albumin (BSA)–loaded ASSP-MPs (Fig. 4, A and B). Quantification analysis indicated a marked signal decrease in both aMSCs and ASSP-MPs at 1 day, and there was a subsequent continuous decline in signal from aMSCs, whereas the signal from ASSP-MPs remained relatively steady over time. At 14 days, 39.4 ± 3.5% of the initial ASSP-MPs signal still remained within the ischemic site; in contrast, the signal of aMSCs was negligible at this time point.

ASSP-MPs therapy for acute HI

We next sought to test whether ASSP-MPs were capable of promoting in vivo regeneration of vascular networks and blood perfusion using an acute HI model. The following five interventions were analyzed by one-dose intramuscular administration: (i) PBS, (ii) BSA-loaded PLGA-MPs (PLGA-MP-BSA), (iii) 3D-CF, (iv) 2D-aMSCs, and (v) ASSP-MPs. Blood perfusion of ischemic muscle was determined by using a laser Doppler perfusion imaging system (Fig. 4C). No obvious signal changes of blood perfusion were seen in normal limbs (right legs) over time, but there were marked decreases for those of the limbs subjected to ischemic surgery within 2 hours. Quantification analysis revealed that the regional blood flow had abruptly declined to approximately 20% of normal levels under all conditions following ischemic surgery, as expected (Fig. 4D). The mice treated with PBS led to a slow increase in blood flow to the tissue over time. The injection of other controls, PLGA-MP-BSA and 3D-CF, resulted in no significant differences, compared to the PBS group. In contrast, ASSP-MPs led to the recovery to nearly 100% blood perfusion compared to normal limbs and a 1.5 ± 0.4–fold increase in blood perfusion compared with 2D-aMSC treatments, at the experiment end point ($P < 0.05$). The level of hindlimb loss and tissue necrosis at 21 days was also quantified by visual observation (Fig. 4E). HI resulted in severe necrosis and foot loss of all animals in PBS and PLGA-MP-BSA treatment groups but treatment with 3D-CF, 2D-aMSCs, and ASSP-MPs protected the limbs from necrosis. In particular, animals treated with ASSP-MPs showed impressive tissue regeneration capacity, with more than 80% salvaged HI and less than 20% necrosis observed.

We next evaluated multiple parameters of tissue sections isolated from muscle tissues at 21 days after surgery. Immunostaining of tissue sections for CD31, an endothelial cell marker, showed blood vessel distribution in muscle tissue (Fig. 4F). Quantification of blood vessel densities revealed that compared to untreated animals, significant decreases in vessel densities were observed for the mice treated with PBS ($P < 0.01$), PLGA-MP-BSA ($P < 0.05$), 3D-CF ($P < 0.05$), and 2D-aMSCs. ASSP-MP treatments increased vessel densities by 11.2-, 8.6-, and 5.3-fold, as compared with PBS, PLGA-MP-BSA, and 3D-CF treatments, respectively (Fig. 4G). Compared to the animals treated with PBS and PLGA-MP-BSA, ASSP-MPs revealed markedly reduced apoptosis, inflammatory cell infiltration, and fibrosis by evaluation with terminal deoxynucleotidyl transferase–mediated deoxyuridine triphosphate nick end labeling (TUNEL) immunostaining assay (Fig. 4H and fig. S7A), hematoxylin and eosin (H&E) staining (Fig. 4I and fig. S7B), and Masson's trichrome staining (Fig. 4J and fig. S7C), respectively, with ASSP-MP–treated tissue composition being comparable to that seen in normal healthy tissues.

Reconstruction of artificial 3D SSP using PLGA nanoparticles (ASSP-NPs)

Cell membranes derived from different cells have shown varied benefits in designing biomimetic nanomedicine (*29*). For example, coating red blood cell (RBC) membranes (RCMs) onto nanoparticle surfaces effectively camouflaged the nanoparticles and led to their prolonged blood circulation (*30*), whereas the use of platelet membranes (PMs) to coat nanoparticle surfaces enhanced the capability of nanoparticles to target sites of vascular injury (*31*). In addition, nanoscale particles were capable of targeted to acute ischemic tissues, due to the increased vessel permeability that accompanies ischemic conditions (*32*), in a similar manner to the enhanced permeability and retention effect of tumors. To construct an ASSPs capable of targeting ischemic tissues via systemic delivery, we further designed and synthesized nanosized ASSPs, as outlined in Fig. 5A. For this delivery platform, we used both RCMs and PMs to coat onto nanosized PLGA particles that encapsulated CF secreted from 3D SSPs (ASSP-NPs). Transmission electron microscopy (TEM) imaging showed the presence of membrane structures on the particle surfaces, according to negative staining (Fig. 5B). After cell membrane coating, the size of the particles remained stable in solution over time, with an approximate average size of 125 nm (Fig. 5C). However, there was a change in the measured ζ potential, which changed from −58 to −29 mV (Fig. 5D). Confocal imaging revealed that both RCMs (red) and PMs (blue) were present on all fluorescein isothiocyanate (FITC)–loaded PLGA nanoparticles (PLGA-NPs) (Fig. 5E). SDS-PAGE analysis of the extracted cell membranes showed that when the membranes were mixed and coated onto nanoparticle surfaces, there was an even distribution of proteins that were present in both membrane types (Fig. 5F), further confirming the successful dual coating of cell membranes onto the nanoparticles. The loading efficiency of 3D-CF was approximately 45.7 ± 3.8%. Following coating with cell membranes, the ASSP-NPs maintained their CF release kinetics, similar to 3D-CF–containing PLGA-NPs (Fig. 5G).

ASSP-NP therapy in an acute MI model

Before evaluation of ASSP-NP therapeutic effects, we assessed whether ASSP-NPs could target/home to ischemic tissues when injected intravenously in an acute MI model. Ex vivo fluorescent imaging revealed that the particles mainly distributed in the liver and kidney regardless of sham and MI mice (fig. S8), which were results similar to those in a previous study (*19*). Compared to the sham heart (without MI surgery), there was an elevated signal from particles that had remained within the MI heart, 1 hour after tail vein injection of Cy5-loaded ASSP-NPs (Fig. 6A). When increased to 6 and 24 hours after injection, the signal intensity of MI heart was 2.8-fold ($P < 0.01$) and 4.5-fold ($P < 0.01$) higher than sham heart at the same time points, respectively. Histology further confirmed significantly increased numbers of injected particles in the tissues isolated from the heart ischemic region, showing accumulated distribution in the ischemic tissues (Fig. 6B).

We next sought to explore the capacity for ASSP-NPs to achieve functional recovery in mice with acute MI. Echocardiographic images showed left ventricular wall motion in mice with or without the indicated treatments at 28 days after surgery (Fig. 6C). Quantification analysis revealed that compared to PBS treatment, there was gradual improvement in the recovery of heart functionality when mice were administered 3D-CF, PLGA-NP-CF (CF loaded into PLGA-NPs without membrane coating), and ASSP-NPs, as evidenced by determining

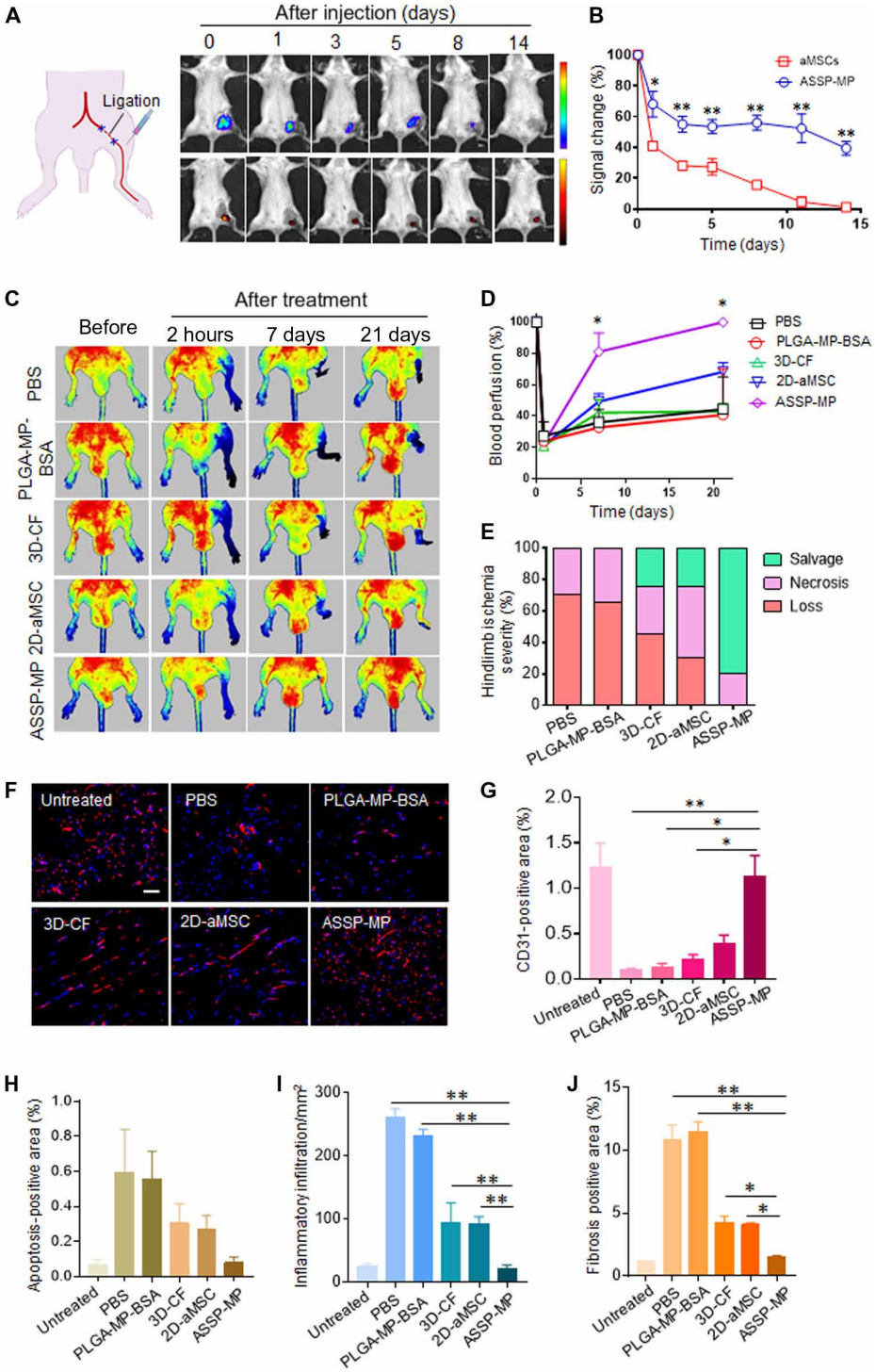

Fig. 4. Retention ability and therapeutic effect of ASSP-MPs in an acute HI model. (**A**) Bioluminescence and fluorescence imaging and (**B**) quantification analysis of signal changes of aMSCs and ASSP-MPs after administration into the HI muscle tissues over time ($n = 3$ for each group). *$P < 0.05$ and **$P < 0.01$. (**C**) Representative laser Doppler perfusion images of mice subjected to HI following different treatments at the indicated time points. The left limbs of mice were subjected to ligation for ischemic surgery, and the right limbs were normal. (**D**) Quantification analysis of limb perfusion at different time points determined by laser Doppler imaging as a percentage of the perfusion before subjection to limb ischemia ($n = 6$ for each group). *$P < 0.05$ (ASSP-MPs versus other treatments). (**E**) Ischemic hindlimbs with different treatments were visually examined to determine the severity of HI at 21 days after ligation. (**F**) Confocal imaging and (**G**) image-based quantification analysis of blood vessels in ischemic muscles by immunostaining with anti-CD31 antibody at 21 days after treatment ($n \geq 3$ for each group). Scale bar, 50 μm. *$P < 0.05$ and **$P < 0.01$. Image-based quantification analysis of (**H**) apoptosis, (**I**) inflammation, and (**J**) fibrosis of the isolated muscles with or without treatments based on the corresponding histostaining assays. *$P < 0.05$ and **$P < 0.01$. All data are presented as means ± SEM. A two-tailed, unpaired Student's *t* test was used to compare between any two groups. One-way ANOVA was used to compare between three or more groups.

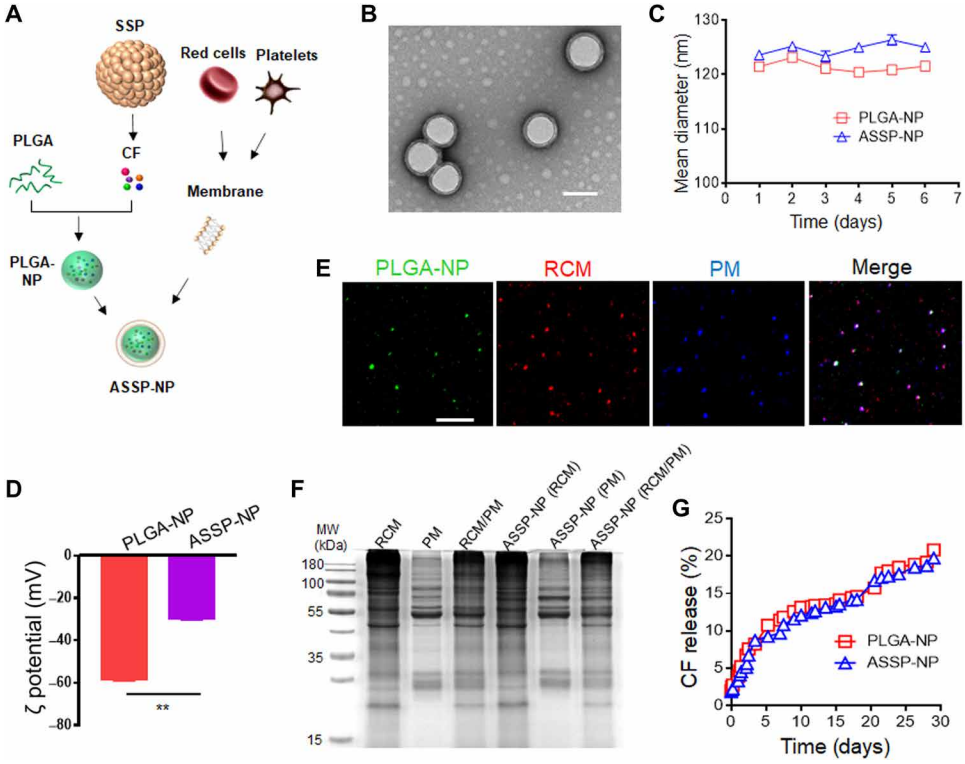

Fig. 5. Preparation and characterization of ASSP-NPs. (**A**) Schematic illustration of the fabrication process of ASSP-NPs. ASSP-NPs were prepared by encapsulating CF secreted from SSPs into PLGA-NPs and the subsequent coating of nanoparticles with RCMs and PMs (i.e., ASSP-NPs). (**B**) TEM imaging of ASSP-NPs after negative staining of the specimen with 1% uranyl acetate. Scale bar, 100 nm. (**C**) Size changes of noncoated PLGA-NPs and membrane-coated ASSP-NPs in PBS solution over time. (**D**) Surface charge change of PLGA-NPs before coating and ASSP-NPs after membrane coating, by measurement of ζ potential. $^{**}P < 0.01$. (**E**) Fluorescent images of the distribution of PLGA-NP core (FITC, green) and membranes (RCMs; DiD, red; PMs, DiI, blue). Scale bar, 5 μm. (**F**) Representative gel image of the protein contents extracted from different cell membranes by SDS-PAGE analysis. (**G**) CF release kinetics from PLGA-NPs and ASSP-NPs incubated in PBS solution. All data are presented as means ± SEM. A two-tailed, unpaired Student's *t* test was used to compare between any two groups.

the parameters of left ventricular ejection fraction (LVEF) and left ventricular fractional shortening (LVFS) (Fig. 6D). Following 28 days of treatment, heart functionality levels in the ASSP-NP treatment group had almost recovered to those measured in sham animals. Next, the hearts were isolated for further evaluation by histological analysis. Masson's trichrome staining displayed the distribution of healthy myocardium (red) and scar (blue) tissue in hearts 28 days after treatment. Figure 6E shows a certain degree of heart damage after acute MI surgery in all mice, especially for PBS group; the left ventricular wall thinned and had a high distribution of scar tissue. Further quantification analysis of infarct thickness and scar area demonstrated that 3D-CF treatments had protective effects, compared to the PBS group, and a similar effect was observed in the PLGA-NP-CF treatment group (Fig. 6F). Moreover, the greatest protective effects were observed in the mice treated with ASSP-NPs, suggesting that membrane coating of nanoparticles could enhanced the delivery of 3D-CF to infarcted hearts. Immunostaining of isolated heart ischemic regions revealed that blood vessel density in the PBS group had decreased to 29.5 ± 3.6% of sham mice (Fig. 6, G and H). Compared to other treatments, ASSP-NP treatments resulted in the significant occurrence of revascularization ($P < 0.05$). Furthermore, H&E staining of major organs suggested that there was no apparent accumulation toxicities or damage to the organs evaluated (fig. S9).

DISCUSSION

In this study, we investigated the benefits of 3D SSPs in improved secretion of proangiogenic CF. On the basis of the advantages of 3D-CF, we introduced biomimetic ASSPs, with readily controllable sizes, which took advantage of the integration of encapsulated CF and cell membrane coatings into PLGA particles. Our developed ASSPs were used to treat two different ischemic diseases, through facile adjustment of size and particle coating. Unlike common 2D culture of stem cells, the CF secreted from 3D SSPs showed significantly superior proangiogenic capacity, and this was mainly due to prosecretion mechanisms regulated by the hypoxic microenvironment contained within spheroid cultures. Our ASSPs have similar functionality and benefits of CF-secretion from 3D SSPs, with the additional advantages provided by surface-coated membrane profiles that are biomimetic to cells suited for disease therapy. Overall, our versatile ASSPs provided (i) adjustable size, dependent on the requirement of medical indication and delivery route, (ii) long-term cryostorage after lyophilization, (iii) prolonged retention/survivability after local transplantation, and (iv) preferential accumulation and targeting to ischemic tissues after systemic delivery. Undoubtedly, not all of these properties are available for stem cells themselves, and thus, our system expands the prospects of stem cell–based therapeutics. Our investigation showed that these benefits combined to provide potent

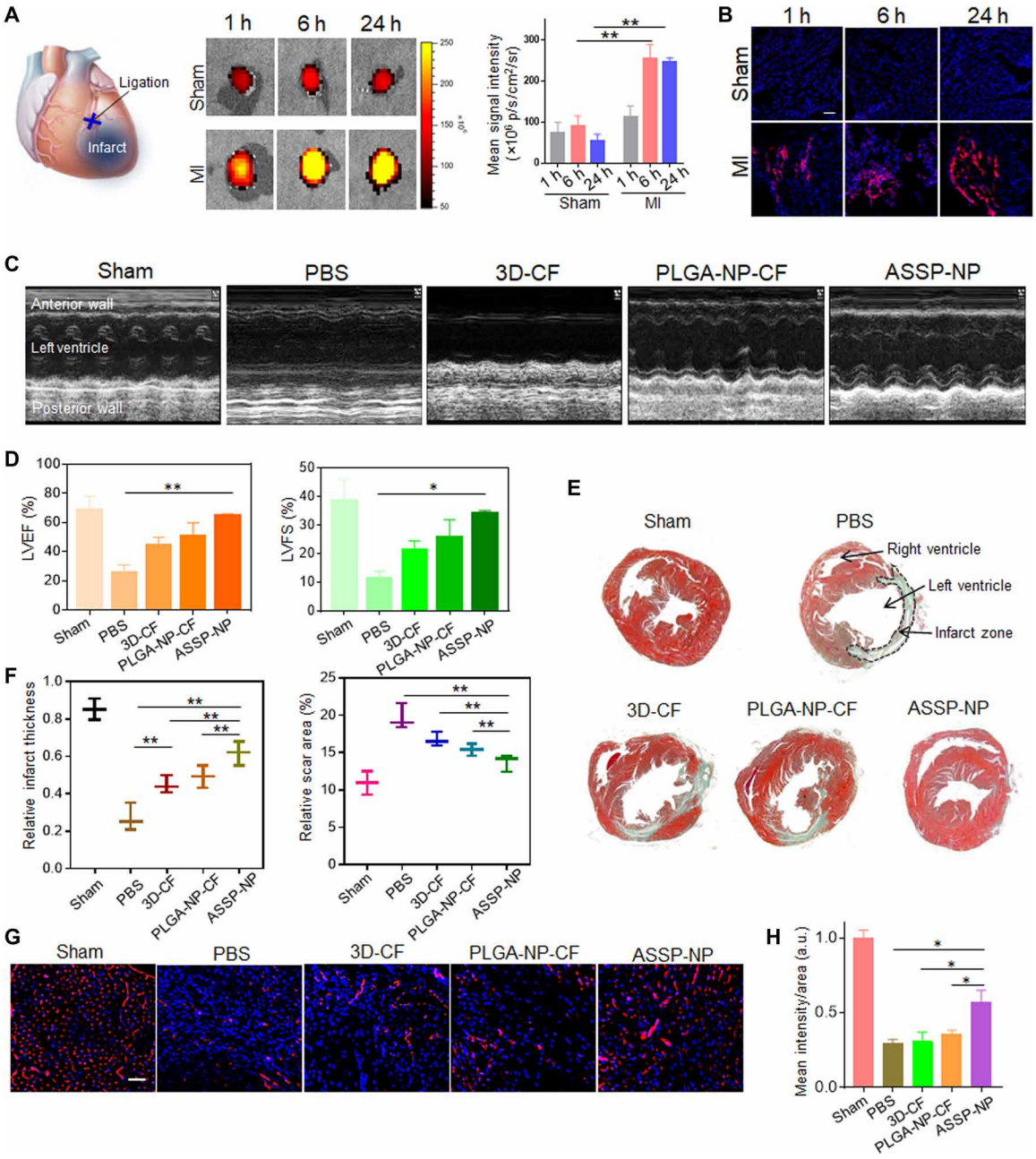

Fig. 6. Accumulation and cardiac repair of ASSP-NPs in a mouse MI model following intravenously administration. (**A**) Representative ex vivo fluorescent imaging of mouse hearts and quantitative analysis of fluorescence intensities at different time points after tail vein injection of ASSP-NPs into sham and MI mice ($n = 3$ for each group). (**B**) Representative images of distribution of ASSP-NPs in nonischemic or ischemic cardiac tissues of the mice following intravenous injection at different time points. Scale bar, 100 μm. (**C**) Representative echocardiographic images of the left ventricular wall motion of mice with or without treatments following MI surgery at 28 days ($n = 5$ for each group). (**D**) Quantification analysis of cardiac function recovery of (C) by determining the parameters of left ventricular ejection fractions (LVEFs) and left ventricular fractional shortening (LVFS). $^*P < 0.05$, $^{**}P < 0.01$. (**E**) Representative images of midpapillary regions of the hearts, 28 days after MI using Masson's trichrome staining (blue, collagen-rich scar tissue; red, viable myocardium). (**F**) Quantitative analysis of (left) infarct wall thickness and (right) scar area of the infarcted hearts with or without treatments ($n \geq 3$ for each group). $^{**}P < 0.01$. (**G**) Representative images and (**H**) image-based quantification analysis of blood vessels in cardiac ischemic regions by immunostaining with anti-CD31 antibody at 28 days after treatments ($n \geq 3$ for each group). $^*P < 0.05$. Scale bar, 50 μm. a.u., arbitrary units. All data are presented as means ± SEM. A two-tailed, unpaired Student's *t* test was used to compare between any two groups. One-way ANOVA was used to compare between three or more groups.

therapeutic efficacy in animal models of HI and MI, with outcomes including enhanced blood perfusion and recovery of heart functionality.

The controlled release of bioactive factors from micro-/nanoparticles in a localized and gradient-style manner can offer strategies to mimics the paracrine communication of cells (*33*). The delivery of bioactive factors alone (e.g., VEGF) has been proven to be an effective strategy to induce angiogenesis. However, drawbacks include unregulated growth factor administration, such as increased vascular leakiness, the induction of proinflammatory reactions, and the promotion of tumor growth (*34*–*37*). A major reason for these outcomes can be

explained by growth factor overload, which is not conducive to the sequential process of blood vessel formation, wherein neovascularization is not mediated by only one specific factor but by the synergistic actions of various angiogenesis factors (i.e., CF). The stress response to hypoxia serves as a major upstream driving power of endogenous angiogenesis (*38*, *39*) and is a status associated with ischemic tissues (*40*). Typically, hypoxic cells secrete various factors to initiate angiogenesis by inducing tip cell formation for new vascular sprouts. This process is dependent on gradients of soluble proangiogenic factors secreted by hypoxic cells. Thus, the factors secreted from hypoxic cells make an appropriate choice when devising biomimetic approaches to inducing angiogenesis. In this work, our constructed 3D SSPs exhibited internal hypoxic microenvironments (Fig. 2, B and C), and thus, the production of angiogenic factors by the hypoxic core cells (Fig. 2, D and E) was an effective and well-controlled guarantee to ensure that gradients of growth factor production induced by hypoxic conditions were within the physiological range required to induce neoangiogenesis. When 3D-CF was released from ASSPs in a controlled manner, the CF was readily able to meet the requirements to stimulate the sequential stages of new vessel formation. In vitro results further demonstrated that the resulting 3D-CF promoted revascularization through a positively modulating endothelial cell behavior (Fig. 2, F and G). Reconstructed ASSPs conveyed these revascularization effects when used in in vivo ischemic disease models (Figs. 4F and 6G). The protein factors released by stem cells in a paracrine fashion have been shown to modulate complex therapeutic actions, including, but not limited to, angiogenesis (*41*, *42*). Compared to 2D cell culture, hypoxia-induced CF secreted by our constructed 3D SSPs mainly included proangiogenic factors, as evidenced by proteomics analysis, although inflammation- and apoptosis-related factors also had increased production (Fig. 2D). Our results suggested that the culture conditions of SSPs used in this study are more inclined to result in a CF secretion that is proangiogenic. However, the increased inflammation- and apoptosis-related proteins present in 3D-CF and their controlled release from ASSP particles may have conveyed additional beneficial effects that we did not explore in the current investigation. In addition, given the broad range of biological and physiological functions that stem cell secretory profiles can regulate, it can be speculated that modification of culture conditions (e.g., inclusion of a cell or biomaterial feeder layer) may be conducive to priming SSPs to secrete CF more beneficial to a broader range of disease conditions, such as the forced induction of anti-inflammatory or prosurvival factors.

An ideal biomimetic therapeutic agent is one that is capable of capturing the tailored and optimized biological profiles according to the requirement of the targeted disease. In the present study, we addressed two demands that were determined by the feasibility of local injection for the sustained treatment of acute HI and systemic delivery for the targeted treatment of acute MI. The reasons that stem cell delivery is ineffective for these applications include the following: (i) The limited delivery efficacy of stem cells remains a bottleneck issue in the progression of cellular approaches, owing to inevitable entrapment of stem cells within lung tissue following systemic administration (*10*, *11*, *19*); (ii) direct injection into the myocardium is a high-risk procedure, where noninvasive delivery is more preferential; and (iii) poor retention of stem cells and their low engraftment survival rate within the myocardium limit direct cell injection as an option for MI (*18*). Reconstructed ASSPs with cell membrane coatings resolved the above shortfalls of stem cell delivery, particularly through the freely adjustable size of ASSPs (Figs. 3A and 5A). The use of membrane coatings on particles granted the improved potential to stimulate ASSP-resident cell interactions, to be camouflaged against rapid blood clearance and to target damaged and activated endothelium. For example, ASSP-NPs fused with RBC/platelet hybrid membranes significantly improved MI heart accumulation, mainly resulting from RBC properties of enhanced circulation half-life and platelet-mediated binding to injured endothelium through recognition of various surface receptor–ligand interactions such as glycoproteins: (GP)VI, GPIV, GPIb, GPIX, GPV, and GPIIb/IIIa (*18*, *43*, *44*). Thus, the use of various types of cell membrane for different types of tailored regenerative treatments is an exciting field that warrants further investigation in conjunction with future ASSPs and biomaterial development. The therapeutic efficacy of these kind of biomimetic artificial cells was similar to the engraftment of stem cells themselves (*16*, *17*) and, in some cases, improved revascularization, when compared to aMSC treatment, especially following engraftment into HI models (Fig. 4). Our versatile artificial cell systems offer an expansion to stem cell–based approaches by linking material science with regenerative medicine.

MATERIALS AND METHODS

Synthesis and purification of PEG-RGD

A typical synthesis procedure of PEG-RGD was used and was described as follows. Briefly, 100 mg of eight-armed PEG-COOH (molecular weight, 10,000 JenKem Technology), 23 mg of 1-ethyl-3-(3′-dimethylaminopropyl)carbodiimide, and 13.8 mg of *N*-hydroxysuccinimide were dissolved into 5 ml of dimethylformamide (DMF) and stirred overnight in an ice bath. RGD molecules (27.7 mg; Shanghai Top-peptide Biotechnology) was then added at a 8:1 molar ratio of RGD:PEG-COOH and stirred for an additional 24 hours at room temperature. Unreacted RGD and DMF were removed by dialysis using CelluSepH1-membrane (molecular weight cutoff, 3500 Da; Beijing GENIA Biotechnology) against deionized water for 12 hours. PEG-RGD was lyophilized to obtain the final product. The conjugation efficiency of RGD was analyzed using an elemental analyzer (Elementar), and it was demonstrated that two to three RGDs were conjugated into each of the eight-armed PEG molecules.

aMSC culture and identification

Adipose tissue, from the peritoneal and inguinal sites, was extracted from healthy BALB/c mice (Vital River) of approximately 8 weeks of age and was rinsed three times with PBS solution containing 2% penicillin/streptomycin (Thermo Fisher Scientific). Under sterile conditions, adipose tissue was minced and digested with 0.075% type I collagenase for 10 min at 37°C. The samples were then neutralized with complete medium and centrifuged at 1600 rpm for 5 min. The supernatant including floating adipocytes was discarded. The pellet containing the aMSC fraction was resuspended and seeded with culture medium, which consisted of 80% α-modification minimum essential medium (Thermo Fisher Scientific), 20% fetal bovine serum (Gibco), and 1% penicillin/streptomycin. The aMSCs were incubated at 37°C with 5% CO_2, and half of the medium was replaced every 3 days. After three passages, the aMSCs were harvested for identification. Approximately 3×10^5 cells were suspended in PBS and incubated with fluorescence-conjugated antibodies [CD29-FITC, CD31-FITC, CD34-FITC, CD44–phycoerythrin (PE), CD45-PE,

CD73-PE, CD90-PE, CD105-PE, and Sca-1–PE] at 37°C for 1 hour (all antibodies were purchased from BioLegend). After two washes with PBS, the cells were analyzed by flow cytometry (BD Biosciences). For adipogenic and osteogenic differentiation, the cells were cultured with adipogenic differentiation medium (Invitrogen) for 2 weeks and with osteogenic differentiation medium (Invitrogen) for 3 weeks, respectively. After fixation with 4% paraformaldehyde, the cells were stained with Oil Red O (Sigma-Aldrich) for 15 min at room temperature to assess adipogenic differentiation and with Alizarin Red S (Sigma-Aldrich) for 30 min at 37°C to visualize osteogenic differentiation, respectively. The cells were washed three times with PBS, and the images were captured using light microscopy (Olympus).

Preparation of 3D SSPs and CF

To prepare 3D SSPs, an optimal condition was determined by adding different concentration (0 to 5 mg/ml) of 8-PEG-RGD into the culture medium containing aMSCs (5×10^5/ml), corresponding to the relative control treatments. The cell suspension was incubated using gentle rotational stirring at 37°C for 1 hour. The formation of aggregates was observed in the cells treated with 8-PEG-RGD. The cell suspension were then plated onto six-well plate containing 1% agarose gel (Thermo Fisher Scientific) and cultured overnight. The medium was subsequently replaced with serum-free medium (2 ml per well) and continued to culture for CF collection. The optimized concentration of 8-PEG-RGD was determined as 5 mg/ml by evaluating the morphology and diameter of the resulting spheroids under microscopy observation (fig. S2). To evaluate 3D structure of SSPs, the cells involved in SSPs were labeled with CellTracker Probes (Thermo Fisher Scientific) for 30 min, followed by 4′,6-diamidino-2-phenylindole (DAPI; Solarbio) for 15 min. The Z-stack imaging of SSPs was performed using confocal laser scanning microscopy (Zeiss). 3D structure of SSPs was determined by the reconstructed 3D images under the corresponding Zeiss software. For the microscopic observation of hypoxia in SSPs, pimonidazole HCl (200 μM; Hypoxyprobe) was added to the SSPs and incubated for 2 hours before cryosection and immunostaining using the Hypoxyprobe-1 Kit (Hypoxyprobe), following the manufacturer's instruction. For analysis of mRNA expression level of various proangiogenesis factors, the samples extracted from aMSCs and 3D SSPs were evaluated by the semiquantitative real-time polymerase chain reaction (Eppendorf). The sequences of primers for proangiogenic factors assessed are listed in table S1.

The same number of aMSCs (5×10^5/ml) was seeded into 2D and 3D culture system containing 2 ml of serum-free medium. Under serum-free medium culture condition, the cell number was monitored over time by cell counting analysis. Given no significant difference in cell number (fig. S3), the medium with CF secreted from aMSCs or 3D SSPs (i.e., conditioned medium) was collected 5 days after culture in serum-free medium. The medium was filtered through a 0.22-μm filter into a sterile centrifuge tube to remove any cell debris and contaminants. The protein concentration of the final CF from 2D and 3D culture was ~0.35 and ~1.1 mg/ml, respectively. Sterile CF was stored at −80°C until further experimentation. The resulting CF was analyzed using proteomic technology by the service of PTM Biolab Inc. (Hangzhou, China). The differences in protein content between 2D-CF and 3D-CF were compared by LC-MS proteomic analysis. Differentially expressed proteins were defined as those in which the average LFQ intensity for each group exceeded a twofold change, with a P value of less than 0.05. For function comparison, an unsupervised enrichment analysis between the two groups of differentially expressed proteins was examined using the KEGG pathway database.

In vitro functional vascularization assays using HUVECs

To assess the impacts of the SSPs on paracrine actions, the migration and tube formation capacity of SSPs on HUVECs were analyzed. The CF-containing conditioned medium (i.e., CF) of 3D SSPs and 2D-aMSCs cultures was collected. For HUVEC transwell migration assays, 2×10^5 HUVECs were cultured in the upper chamber that had 8-μm pore size (Corning). The collected conditioned medium was directly added into the lower chamber. HUVECs were cultured under normal conditions and, with no additional CF treatment, were used as controls. After 12-hour incubation time, migrated cells were fixed, stained, and counted by ImageJ (National Institutes of Health). Tube formation was evaluated by culturing HUVECs in a confocal plate coated with Matrigel (BD Biosciences) with the direct addition of CF-conditioned medium. After 6-hour incubation time, the formed capillary-like structures were stained with FITC-labeled phalloidin (Solarbio) and observed using laser confocal scanning microscopy.

Preparation and characterization of ASSP-MPs

CF-loaded PLGA microparticles (ASSP-MPs) were fabricated using a water/oil/water (w/o/w) emulsion technique. Briefly, the frozen powder of CF was dissolved in 500 μl of 0.1% polyvinyl alcohol (PVA) as the internal aqueous phase [containing 3D-CF (~1.1 mg/ml)], and this was mixed in 6 ml of methylene chloride containing 100 mg of PLGA, which was the oil phase. The mixture was then sonicated on ice at a steady power of 500 W for 25 s. Next, the primary emulsion was immediately introduced into 40 ml of water with PVA to produce a w/o/w emulsion. The secondary emulsion was emulsified at 1500 rpm for 7 min. The w/o/w emulsion was continuously stirred at room temperature for solvent evaporation. The solidified PLGA-MPs were then centrifuged, washed three times with water, lyophilized, and stored at −80°C. The cryopreservation stability was determined by analyzing the fresh and postfreezing/thawing samples.

To extract cell membrane, SSPs were collected from a well of six-well plate in 10 ml of hypotonic lysing buffer consisting of 1 mM $NaHCO_3$, 0.2 mM EDTA, and 1 mM phenylmethylsulfonyl fluoride at 4°C. Then, the suspension was sonicated for 20 min to obtain the membrane fragments. After centrifugation at 3200g for 5 min at 4°C, the resulting supernatant was collected and centrifuged again at 15,000g for 30 min at 4°C. The isolated membranes were dispersed in 100 μl of PBS (pH 7.4) at 4°C for subsequent experiments. The protein concentration of the membrane sample was ~70 μg/ml. For cell membrane coating, SSP cell membrane (4.2 μg, 60 μl) was mixed with 2.5 mg of PLGA-MPs and sonicated for 20 min. The mixture was centrifuged and washed three times to obtain ASSP-MPs. The particle numbers in PBS solution were observed by microscopy and calculated by cell-counting method, with ASSP-MPs (~8×10^5 particles/mg). The surface morphology of PLGA-MPs and ASSP-MPs was observed by scanning electron microscopy (Hitachi). In addition, FITC-labeled BSA was loaded into PLGA-MPs, and cell membranes stained with 1,1'-Dioctadecyl-3,3,3',3'-Tetramethylindodicarbocyanine (DiD) (Solarbio) were coated onto PLGA-MP surfaces. Subsequently, the resulting samples were visualized under confocal laser scanning microscopy. To characterize aMSC, PLGA-MP, and ASSP-MP surface expression of markers, flow cytometry analysis was performed. Briefly, the samples were incubated

with dye-labeled antibodies (CD29-FITC, CD44-PE, CD73-PE, CD90-PE, CD105-PE, and Sca-1–PE) at 37°C for 1 hour. After three washes with PBS, each group was analyzed by flow cytometry.

To determine encapsulation efficiency of CF, the particles were pelleted by centrifugation, and then the nonencapsulated amount of CF in the supernatant was measured using a bicinchoninic acid (BCA) protein assay (Solarbio). The encapsulation efficiency was calculated according to the following equation

$$\text{Encapsulation efficiency (\%)} = \frac{(B - A)}{B} \times 100\%$$

where A is the amount of CF in the supernatant and B is the theoretical loading of CF in the PLGA particles, as calculated from the input amount during the preparation.

In vitro release kinetics

For release assays, particles (4 mg/ml) were incubated in 20 ml of PBS buffer (pH 7.4) at 37°C under gentle stirring at 150 rpm. At the specified time intervals, 100 μl of sample was collected and centrifuged at 4000 rpm for 5 min, and the same amount of fresh PBS was added to replenish the volume. The supernatant was analyzed for protein release as determined by BCA protein assay.

The components in the released solution from ASSP-MPs were evaluated by standard procedures using ELISA kits (Shanghai Enzyme-linked Biotechnology Co. Ltd.). Briefly, the released solution was collected from the particles (20 mg/ml) incubated in 5 ml of PBS buffer. Samples solution (100 μl) was added into precoated 96-well plates with primary antibody and incubated for 1 hour. After washing, the secondary antibodies (i.e., anti-VEGF, anti-IGF, and anti-EGF antibodies) were added for 15-min incubation. The color reactions were subsequently performed, and the absorbance value was acquired by microplate reader at 450 nm.

Acute HI model

All animal studies were approved by the Animal Ethics Committee of Nankai University and followed the Tianjin Committee of Use and Care of Laboratory Animals. Male BALB/c nude mice (20 to 25 g, 8 to 10 weeks old) were used to establish HI models, according to our previously described protocols (*22*). Briefly, mice were anesthetized, and a skin incision was made. The left femoral artery and vein were ligated using 6-0 silk, and a cut was made just above the deep femoral artery to the popliteal artery and vein.

For evaluation of the survival/retention of aMSCs and ASSP-MPs, the luciferase-expressing aMSCs and Cy5-labeled BSA-loaded ASSP-MPs were imaged following local administration into ischemic tissue in an HI model, respectively. Briefly, 100 μl of aMSCs (1×10^6 cells) and ASSP-MPs (1×10^6 particles) were injected into ischemic tissue after the above surgery procedure, respectively. Following the indicated time points, the fluorescence imaging of ASSP-MPs was directly acquired via an in vivo imaging system (IVIS Lumina II Xenogen), whereas the imaging of aMSCs was performed after tail vein injected with D-luciferin for 15 min. The decayed signal intensity was analyzed by comparison with the initial time point.

Following the above surgical procedure, the mice were randomly assigned to five groups to receive intramuscular injections with 100 μl of solution, containing PBS, PLGA-MP-BSA (1×10^6 particles), CF (containing the equivalent amount of CF as the ASSP-MP group), 2D-aMSCs (1×10^6 cells), or ASSP-MPs (1×10^6 particles). Laser Doppler imaging (PeriCam PS24 System, Perimed AB) was conducted to quantitatively detect the subcutaneous blood flow within hindlimbs at the designated time points. The average values of blood perfusion were subsequently calculated using the PeriCam PSI System. The score of limb salvage, necrosis, and loss in treatment groups was also quantified by visual observation following previously method (*45*). Tissue damage in the ischemic limb (limb salvage score) was graded as salvage (grade 6), necrosis (grade 2 to grade 5), and loss (grade 1). The percentage of salvage, necrosis, and loss for ischemic limb was quantified, respectively.

Muscle tissues were harvested from the mice subjected to acute HI at the designated time points. Histochemical and histopathological staining assays were performed following standard procedures. Briefly, apoptosis and angiogenesis of tissues were performed by staining of cryosections using TUNEL staining method (Roche) and anti–CD31-PE antibody (BioLegend), respectively. Inflammatory infiltration of muscle and fibrosis formation was examined by H&E and Masson's trichrome staining, respectively. The images of the stained tissues from different treated mice ($n \geq 3$, at least five cryosections each mouse) were acquired, and image-based quantification analysis was performed on ImageJ software. The blood vessel, apoptosis, and fibrosis in muscle samples were quantified by evaluation of their positive area percentage in the stained muscle tissues. The inflammatory infiltration was determined by calculating inflammatory cell number/area in the stained tissue.

Preparation of PLGA-NPs

PLGA-NPs were prepared following the below procedure. Briefly, the conditioned medium was used as internal aqueous phase [containing 3D-CF (~2.2 mg/ml)] and was mixed in 5 ml of methylene chloride containing 100 mg of PLGA oil phase. The mixture was then sonicated on ice at a steady power of 200 W for 40 s using a microtip probe. Next, the primary emulsion was immediately introduced into 10 ml of 1% sodium cholate hydrate, emulsified under sonication at 200 W for 120 s, and then mixed with 15 ml of 0.5% sodium cholate hydrate, which resulted in the final PLGA-NP emulsion. The emulsion was continuously stirred at room temperature for 5 hours for solvent evaporation. The solidified nanoparticles were then centrifuged (12,000 rpm for 10 min) and washed with water.

Cell membranes isolation and coating of PLGA-NPs to form ASSP-NPs

The membrane from RBCs and platelets were isolated following previous procedures (*30*, *31*). Whole blood from C57 mice was isolated and centrifuged at 200*g* for 20 min at 4°C. The platelet rich plasma was located in the supernatant, the white blood cells within the middle layer and the RBCs were in the bottom layer. Platelets were then collected from the platelet rich plasma by centrifugation at 800*g* for 20 min at 4°C, and the resulting pellet was resuspended in PBS containing 1 mM EDTA·2Na. The resulting platelet suspension was sonicated for 10 min using a sonicator at a power of 40% to obtain the PM fragments. RBC membrane was extracted from the bottom layer. Briefly, the bottom layer was centrifuged at 800*g* for 5 min at 4°C and washed three times with ice-cold PBS to remove the residual plasma and the buffy coat. To remove the intracellular contents of RBC, the washed RBC was suspended in water with 1 mM EDTA·2Na in an ice bath overnight and subsequently centrifuged at 6000*g* for 10 min. After removing the hemoglobin, the pink pellet (i.e., RBC membrane) was collected. The membrane fragments were obtained by sonication for 10 min using a sonicator at a power of 40%.

To coat cell membrane onto PLGA-NPs, RCMs (containing 12.5 μg of protein) was added to PMs at a membrane protein weight ratio of 1:1; this was followed by sonication for 10 min using a water bath sonicator and stirring at 37°C for 10 min to facilitate membrane fusion. The mixture was added into 1 ml of PLGA-NPs (4 mg/ml) and, subsequently, was extruded 20 times through a 400-nm polycarbonate porous membrane using an Avanti mini extruder to form the final coated nanoparticles (i.e., ASSP-NPs). The encapsulation efficacy of 3D-CF was calculated by the same formula as ASSP-MPs. The membrane structures on ASSP-NPs were observed by TEM (Hitachi) after negative staining of the specimen with 1% uranyl acetate. In addition, PLGA-NPs, RCMs, and PMs were labeled with FITC, DiD, and 3,3'-Dioctadecyloxacarbocyanine (DIO), respectively, for observation with confocal microscopy. Nanoparticle size and ζ potential were measured by dynamic light scattering using a Zetasizer (Mastersizer 2000, Malvern).

Acute MI model

The method to induce MI in mice was followed as in our previous reports (*46*). Briefly, female C57 mice were anesthetized (3% isofluorane combined with 2% oxygen) without mechanical ventilation. Under sterile conditions, a small skin cut was operated over the left chest for exposure of the heart, by minimally invasive left thoracotomy. The acute MI model was made by permanent ligation of the left anterior descending coronary artery. After ligation, the heart was immediately put back into the intrathoracic space, and then the skin was stitched together with suture. The mice were closely monitored until recovery of consciousness.

For imaging of ASSP-NPs accumulation into MI hearts, fluorescent dye–loaded ASSP-NPs were first prepared by replacing CF with Cy5 dyes (0.02 mg/ml). After 24 hours of acute MI induction, the mice subjected to sham and MI received intravenous injections of Cy5-loaded ASSP-NPs (40 mg/kg). At the designated time points, the hearts and other organs were isolated, and ex vivo imaging was acquired using an IVIS Spectrum imaging system (Xenogen). Next, hearts were frozen in optimum cutting temperature compound in preparation for cryosection. The slices were stained using the nuclear stain DAPI and then were observed by confocal microscopy.

For the therapeutic evaluation, the mice were randomly assigned in five groups: sham, PBS, 3D-CF (1.2 mg/kg per dose), PLGA-NP-CF (equivalent amount of CF to the 3D-CF group), and ASSP-NPs (containing equivalent amount of 3D-CF). The treatments were administrated by tail vein injection 24 hours after surgery. The additional three doses were injected every 1 week. Heart function was evaluated 28 days after injection. Cardiac functions were evaluated by transthoracic echocardiography using the VisualSonics Vevo 2100 Imaging System (RMV-707B). Hearts were imaged in long-axis views at the level of the greatest left ventricular diameter. The cardiac functional parameters, including the LVEFs and LVFS, were quantified by the imaging system and built-in software (Vevo770 V3.0.0). Next, hearts were collected for histological analysis following standard staining procedures. Briefly, angiogenesis of tissues was visualized by immunostaining with anti–CD31-PE antibody. Scar formation of all the hearts ($n = 5$) was examined by Masson's trichrome staining. Images were acquired by light microscopy and image-based analysis related to infarct thickness, and scar size was performed on ImageJ software.

Statistical analysis

A two-tailed, unpaired Student's *t* test was used to compare between any two groups. One-way analysis of variance (ANOVA) was used to compare between three or more groups. Differences were considered statistically significant at $P < 0.05$. Results were shown as the means ± SEM.

SUPPLEMENTARY MATERIALS

Supplementary material for this article is available at http://advances.sciencemag.org/cgi/content/full/6/19/eaaz8011/DC1

View/request a protocol for this paper from *Bio-protocol*.

REFERENCES AND NOTES

1. G. W. Reed, J. E. Rossi, C. P. Cannon, Acute myocardial infarction. *Lancet* **389**, 197–210 (2017).
2. A. Farber, R. T. Eberhardt, The current state of critical limb ischemia: A systematic review. *JAMA Surg* **151**, 1070–1077 (2016).
3. P. Yan, Q. Li, L. Wang, P. Lu, K. Suzuki, Z. Liu, J. Lei, W. Li, X. He, S. Wang, J. Ding, P. Chan, W. Zhang, M. Song, J. C. Izpisua Belmonte, J. Qu, F. Tang, G. H. Liu, FOXO3-engineered human ESC-derived vascular cells promote vascular protection and regeneration. *Cell Stem Cell* **24**, 447–461.e8 (2019).
4. L. R. Fiedler, K. Chapman, M. Xie, E. Maifoshie, M. Jenkins, P. A. Golforoush, M. Bellahcene, M. Noseda, D. Faust, A. Jarvis, G. Newton, M. A. Paiva, M. Harada, D. J. Stuckey, W. Song, J. Habib, P. Narasimhan, R. Aqil, D. Sanmugalingam, R. Yan, L. Pavanello, M. Sano, S. C. Wang, R. D. Sampson, S. Kanayaganam, G. E. Taffet, L. H. Michael, M. L. Entman, T. H. Tan, S. E. Harding, C. M. R. Low, C. Tralau-Stewart, T. Perrior, M. D. Schneider, MAP4K4 inhibition promotes survival of human stem cell-derived cardiomyocytes and reduces infarct size in vivo. *Cell Stem Cell* **24**, 579–591.e12 (2019).
5. S. J. Lee, Y. D. Sohn, A. Andukuri, S. Kim, J. Byun, J. W. Han, I. H. Park, H. W. Jun, Y. S. Yoon, Enhanced therapeutic and long-term dynamic vascularization effects of human pluripotent stem cell-derived endothelial cells encapsulated in a nanomatrix gel. *Circulation* **136**, 1939–1954 (2017).
6. J. Mayourian, T. J. Cashman, D. K. Ceholski, B. V. Johnson, D. Sachs, D. A. Kaji, S. Sahoo, J. M. Hare, R. J. Hajjar, E. A. Sobie, K. D. Costa, Experimental and computational insight into human mesenchymal stem cell paracrine signaling and heterocellular coupling effects on cardiac contractility and arrhythmogenicity. *Circ. Res.* **121**, 411–423 (2017).
7. M. Gartz, J. L. Strande, Examining the paracrine effects of exosomes in cardiovascular disease and repair. *J. Am. Heart Assoc.* **7**, e007954 (2018).
8. C. M. Madl, S. C. Heilshorn, H. M. Blau, Bioengineering strategies to accelerate stem cell therapeutics. *Nature* **557**, 335–342 (2018).
9. Z. Li, S. Hu, K. Cheng, Chemical engineering of cell therapy for heart diseases. *Acc. Chem. Res.* **52**, 1687–1696 (2019).
10. X. Huang, F. Zhang, H. Wang, G. Niu, K. Y. Choi, M. Swierczewska, G. Zhang, H. Gao, Z. Wang, L. Zhu, H. S. Choi, S. Lee, X. Chen, Mesenchymal stem cell-based cell engineering with multifunctional mesoporous silica nanoparticles for tumor delivery. *Biomaterials* **34**, 1772–1780 (2013).
11. X. Huang, F. Zhang, Y. Wang, X. Sun, K. Y. Choi, D. Liu, J. S. Choi, T. H. Shin, J. Cheon, G. Niu, X. Chen, Design considerations of iron-based nanoclusters for noninvasive tracking of mesenchymal stem cell homing. *ACS Nano* **8**, 4403–4414 (2014).
12. Kshitiz, D. D. Ellison, Y. Suhail, J. Afzal, L. Woo, O. Kilic, J. Spees, A. Levchenko, Dynamic secretome of bone marrow-derived stromal cells reveals a cardioprotective biochemical cocktail. *Proc. Natl. Acad. Sci. U. S. A.* **116**, 14374–14383 (2019).
13. W. L. Murphy, T. C. McDevitt, A. J. Engler, Materials as stem cell regulators. *Nat. Mater.* **13**, 547–557 (2014).
14. A. C. Midgley, Y. Wei, Z. Li, D. Kong, Q. Zhao, Nitric-oxide-releasing biomaterial regulation of the stem cell microenvironment in regenerative medicine. *Adv. Mater.* **32**, e1805818 (2019).
15. B. Trappmann, B. M. Baker, W. J. Polacheck, C. K. Choi, J. A. Burdick, C. S. Chen, Matrix degradability controls multicellularity of 3D cell migration. *Nat. Commun.* **8**, 371 (2017).
16. L. Luo, J. Tang, K. Nishi, C. Yan, P. U. Dinh, J. Cores, T. Kudo, J. Zhang, T. S. Li, K. Cheng, Fabrication of synthetic mesenchymal stem cells for the treatment of acute myocardial infarction in mice. *Circ. Res.* **120**, 1768–1775 (2017).
17. J. Tang, D. Shen, T. G. Caranasos, Z. Wang, A. C. Vandergriff, T. A. Allen, M. T. Hensley, P. U. Dinh, J. Cores, T. S. Li, J. Zhang, Q. Kan, K. Cheng, Therapeutic microparticles functionalized with biomimetic cardiac stem cell membranes and secretome. *Nat. Commun.* **8**, 13724 (2017).
18. J. Tang, T. Su, K. Huang, P. U. Dinh, Z. Wang, A. Vandergriff, M. T. Hensley, J. Cores, T. Allen, T. Li, E. Sproul, E. Mihalko, L. J. Lobo, L. Ruterbories, A. Lynch, A. Brown, T. G. Caranasos, D. Shen, G. A. Stouffer, Z. Gu, J. Zhang, K. Cheng, Targeted repair of heart injury by stem cells fused with platelet nanovesicles. *Nat. Biomed. Eng.* **2**, 17–26 (2018).
19. H. Liang, K. Huang, T. Su, Z. Li, S. Hu, P. U. Dinh, E. A. Wrona, C. Shao, L. Qiao, A. C. Vandergriff, M. T. Hensley, J. Cores, T. Allen, H. Zhang, Q. Zeng, J. Xing, D. O. Freytes, D. Shen, Z. Yu, K. Cheng, Mesenchymal stem cell/red blood cell-inspired nanoparticle

therapy in mice with carbon tetrachloride-induced acute liver failure. *ACS Nano* **12**, 6536–6544 (2018).
20. M. W. Laschke, M. D. Menger, Life is 3D: Boosting spheroid function for tissue engineering. *Trends Biotechnol.* **35**, 133–144 (2017).
21. D. Ding, D. Mao, K. Li, X. Wang, W. Qin, R. Liu, D. S. Chiam, N. Tomczak, Z. Yang, B. Z. Tang, D. Kong, B. Liu, Precise and long-term tracking of adipose-derived stem cells and their regenerative capacity via superb bright and stable organic nanodots. *Acs Nano* **8**, 12620–12631 (2014).
22. X. Wang, J. Zhang, W. Cui, Y. Fang, L. Li, S. Ji, D. Mao, T. Ke, X. Yao, D. Ding, G. Feng, D. Kong, Composite hydrogel modified by IGF-1C domain improves stem cell therapy for limb ischemia. *ACS Appl. Mater. Interfaces* **10**, 4481–4493 (2018).
23. L. L. Cui, F. Nitzsche, E. Pryazhnikov, M. Tibeykina, L. Tolppanen, J. Rytkönen, T. Huhtala, J. W. Mu, L. Khiroug, J. Boltze, J. Jolkkonen, Integrin $\alpha 4$ overexpression on rat mesenchymal stem cells enhances transmigration and reduces cerebral embolism after intracarotid injection. *Stroke* **48**, 2895–2900 (2017).
24. R. J. D. Hatley, S. J. F. Macdonald, R. J. Slack, J. le, S. B. Ludbrook, P. T. Lukey, An αv-RGD integrin inhibitor toolbox: Drug discovery insight, challenges and opportunities. *Angew. Chem. Int. Ed. Engl.* **57**, 3298–3321 (2018).
25. W. Dai, J. Belt, W. M. Saltzman, Cell-binding peptides conjugated to poly(ethylene glycol) promote neural cell aggregation. *Biotechnology* **12**, 797–801 (1994).
26. A. Facciabene, X. Peng, I. S. Hagemann, K. Balint, A. Barchetti, L.-P. Wang, P. A. Gimotty, C. B. Gilks, P. Lal, L. Zhang, G. Coukos, Tumour hypoxia promotes tolerance and angiogenesis via CCL28 and T_{reg} cells. *Nature* **475**, 226–230 (2011).
27. K. M. Park, S. Gerecht, Hypoxia-inducible hydrogels. *Nat. Commun.* **5**, 4075 (2014).
28. X. Zheng, X. Wang, H. Mao, W. Wu, B. Liu, X. Jiang, Hypoxia-specific ultrasensitive detection of tumours and cancer cells in vivo. *Nat. Commun.* **6**, 5834 (2015).
29. R. H. Fang, A. V. Kroll, W. W. Gao, L. F. Zhang, Cell membrane coating nanotechnology. *Adv. Mater.* **30**, e1706759 (2018).
30. C. M. J. Hu, L. Zhang, S. Aryal, C. Cheung, R. H. Fang, L. Zhang, Erythrocyte membrane-camouflaged polymeric nanoparticles as a biomimetic delivery platform. *Proc. Natl. Acad. Sci. U.S.A.* **108**, 10980–10985 (2011).
31. C.-M. J. Hu, R. H. Fang, K. C. Wang, B. T. Luk, S. Thamphiwatana, D. Dehaini, P. Nguyen, P. Angsantikul, C. H. Wen, A. V. Kroll, C. Carpenter, M. Ramesh, V. Qu, S. H. Patel, J. Zhu, W. Shi, F. M. Hofman, T. C. Chen, W. Gao, K. Zhang, S. Chien, L. Zhang, Nanoparticle biointerfacing by platelet membrane cloaking. *Nature* **526**, 118–121 (2015).
32. J. Kim, L. Cao, D. Shvartsman, E. A. Silva, D. J. Mooney, Targeted delivery of nanoparticles to ischemic muscle for imaging and therapeutic angiogenesis. *Nano Lett.* **11**, 694–700 (2011).
33. M. Ansorge, T. Pompe, Systems for localized release to mimic paracrine cell communication in vitro. *J. Control. Release* **278**, 24–36 (2018).
34. K. Pajusola, J. Künnapuu, S. Vuorikoski, J. Soronen, H. André, T. Pereira, P. Korpisalo, S. Ylä-Herttuala, L. Poellinger, K. Alitalo, Stabilized HIF-1α is superior to VEGF for angiogenesis in skeletal muscle via adeno-associated virus gene transfer. *FASEB J.* **19**, 1365–1367 (2005).
35. Y. Cao, Monotherapy versus combination therapy of angiogenic and arteriogenic factors for the treatment of ischemic disorders. *Curr. Mol. Med.* **9**, 967–972 (2009).
36. S. Pontes-Quero, M. Fernández-Chacón, W. Luo, F. F. Lunella, V. Casquero-Garcia, I. Garcia-Gonzalez, A. Hermoso, S. F. Rocha, M. Bansal, R. Benedito, High mitogenic stimulation arrests angiogenesis. *Nat. Commun.* **10**, 2016 (2019).
37. M. E. J. Reinders, M. Sho, A. Izawa, P. Wang, D. Mukhopadhyay, K. E. Koss, C. S. Geehan, A. D. Luster, M. H. Sayegh, D. M. Briscoe, Proinflammatory functions of vascular endothelial growth factor in alloimmunity. *J. Clin. Invest.* **112**, 1655–1665 (2003).
38. H. K. Eltzschig, D. L. Bratton, S. P. Colgan, Targeting hypoxia signalling for the treatment of ischaemic and inflammatory diseases. *Nat. Rev. Drug Discov.* **13**, 852–869 (2014).
39. C. W. Pugh, P. J. Ratcliffe, Regulation of angiogenesis by hypoxia: Role of the HIF system. *Nat. Med.* **9**, 677–684 (2003).
40. H. K. Eltzschig, T. Eckle, Ischemia and reperfusion—From mechanism to translation. *Nat. Med.* **17**, 1391–1401 (2011).
41. M. Gnecchi, Z. Zhang, A. Ni, V. J. Dzau, Paracrine mechanisms in adult stem cell signaling and therapy. *Circ. Res.* **103**, 1204–1219 (2008).
42. P. R. Baraniak, T. C. McDevitt, Stem cell paracrine actions and tissue regeneration. *Regen. Med.* **5**, 121–143 (2010).
43. G. Lippi, M. Franchini, G. Targher, Arterial thrombus formation in cardiovascular disease. *Nat. Rev. Cardiol.* **8**, 502–512 (2011).
44. D. Dehaini, X. Wei, R. H. Fang, S. Masson, P. Angsantikul, B. T. Luk, Y. Zhang, M. Ying, Y. Jiang, A. V. Kroll, W. Gao, L. Zhang, Erythrocyte-platelet hybrid membrane coating for enhanced nanoparticle functionalization. *Adv. Mater.* **29**, 1606209 (2017).
45. M. J. Webber, J. Tongers, C. J. Newcomb, K. T. Marquardt, J. Bauersachs, D. W. Losordo, S. I. Stupp, Supramolecular nanostructures that mimic VEGF as a strategy for ischemic tissue repair. *Proc. Natl. Acad. Sci. U.S.A.* **108**, 13438–13443 (2011).
46. Y. Liu, X. Ye, L. Mao, Z. Cheng, X. Yao, X. Jia, D. Mao, L. Ou, Z. Li, Y. Che, N. Liu, G. Steinhoff, L. Liu, D. Kong, Transplantation of parthenogenetic embryonic stem cells ameliorates cardiac dysfunction and remodelling after myocardial infarction. *Cardiovasc. Res.* **97**, 208–218 (2013).

Acknowledgments
Funding: This work was supported by the National Natural Science Foundation of China (81830060, 31870999, 91959129, 31771066, 81921004, and 81850410552), the Natural Science Foundation of Tianjin (18JCYBJC40900), National Thousand Young Talents Program, and Nankai University Hundred Young Academic Leaders Program. **Author contributions:** R.Z., J.Z., and X.H. designed the research. R.Z. and W.L. synthesized and characterized the particles. R.Z., W.L., Y.Z., D.Z., H.S., A.K., and H.Z. performed the animal experiments and analyzed the results. R.Z., A.C.M., J.Z., and X.H. wrote the paper. D.K. and X.H. directed the research and provided the financial support. **Competing interests:** All authors declare that they have no competing interests. **Data and materials availability:** All data needed to evaluate the conclusions in the paper are present in the paper and/or the Supplementary Materials. Additional data related to this paper may be requested from the authors.

Submitted 10 October 2019
Accepted 14 February 2020
Published 6 May 2020
10.1126/sciadv.aaz8011

Citation: R. Zhang, W. Luo, Y. Zhang, D. Zhu, A. C. Midgley, H. Song, A. Khalique, H. Zhang, J. Zhuang, D. Kong, X. Huang, Particle-based artificial three-dimensional stem cell spheroids for revascularization of ischemic diseases. *Sci. Adv.* **6**, eaaz8011 (2020).